Geochemistry, Geophysics, Geosystems

Supporting Information for

Long-distance Asthenospheric Transport of Plume-influenced Mantle

J. Hua[1,2], K. M. Fischer[1], E. Gazel[3], E. M. Parmentier[1] and G. Hirth[1]

[1] Department of Earth, Environmental and Planetary Sciences, Brown University, Providence, RI 02906, USA.

[2] Department of Geological Sciences, The University of Texas at Austin, Austin, 78712, USA.

[3] Department of Earth and Atmospheric Sciences, Cornell University, Ithaca, NY, 14853, USA

Contents of this file

Additional Supporting Information (Files uploaded separately)

Introduction

This file contains the supplementary method details for how we pick receiver function phases; convert seismic shear velocity to temperatures; construct the geotherm and estimate the degree of melting for Karacadag basalt samples; and estimate the viscous flow speed for the long-distance transport. This file also includes supplementary figures for the article. Methods used to generate these figures and their interpretation are discussed in the main text. Captions for the supplementary data sets which are uploaded as separate .xlsx files are also included here.

Text S1. Picking algorithms for receiver function phases

The receiver function stack phases were picked with a phase picking algorithm (Hua et al., 2018) that assumes that the phase amplitude at a given depth is the probability that the velocity gradient is located at the depth (Figure S1a). The expected depth from the probability distribution is used to characterize the center of the velocity gradient associated with the phase, and one and half times the standard deviation from the distribution is used to characterize the depth extent of the velocity gradient. However, although the algorithm used in this study is the same as the previous study (Hua et al., 2018), specific parameters for picking differ. To pick the negative receiver function (PVG) phases at 100-150 km depth associated with the onset of melting, each 1D vertical data column in the stack from 70 to 200 km depths was analyzed. To pick the positive phases associated with the lithosphere-asthenosphere boundary, 40 to 100 km depths were analyzed. For picking positive or negative phases, the following criteria were applied to X, where X is the positive amplitude or the absolute value of negative amplitude, respectively. When treating X values as probability distributions, only X values higher than both 0.01 and twice the amplitude of the standard deviation were used (Figure S1a). Locations were classified as lacking a phase if the maximum value of X was less than 0.02, the expected value of X was less than 0.015 or the standard deviation in depth was less than 2.5 km. Since Sp stack standard deviations at LAB depths were often large (Hua, Fischer, Wu, et al., 2020), fewer reliable phases were picked (Figure S1g). Therefore, to provide approximate LAB depth measurements for more of the region, locations without picked phase depths were assigned the average of picked phase depths within 0.3° of latitude and longitude (Figure S1h).

Text S2. Shear velocity (V_S) – Temperature

Isotropic shear velocity structures from two recent full-waveform inversion models were converted to mantle temperature: a local model (Fichtner et al., 2013) and a regional model (Blom et al., 2020) (Figure 2a). The isotropic velocities were obtained by the Voigt average of horizontal V_{SH} and vertical V_{SV} ($\sqrt{\left(2V_{SH}^2 + V_{SV}^2\right)/3}$). Both models were converted to temperature based on a V_S-temperature relationship (Yamauchi & Takei, 2016) with 100 wt. ppm water and the shear modulus dependence based on a prior seismic study (Priestley & McKenzie, 2013) (Figure 2b). The local model (Fichtner et al., 2013) was also converted to temperature using another V_S-temperature relationship (Jackson & Faul, 2010) (Figure S2f).

Using the first relationship (Yamauchi & Takei, 2016) for the conversion, we also tested the effects of assumed wave period, composition, and mantle water content. For the wave period tests (Figure S2b), V_S was first corrected to the assumed period (25, 70 and 100 s) based on the attenuation model used during the full-waveform inversion. Then we used the shear modulus temperature and pressure dependence in the original work (Yamauchi & Takei, 2016) (based on the seismic study of Priestley and McKenzie (2013) with 100 wt. ppm water). When testing the effects of composition (Figure S2c), we assumed a 70 s period and a mantle with 100 wt. ppm water. Then we used the shear modulus temperature and pressure dependence based on the seismic study (Priestley & McKenzie, 2013) or the dependence from a Perple_X (Connolly, 2009) calculation with the selected thermodynamic data and solution model (Stixrude & Lithgow-Bertelloni, 2011) assuming pyrolite or harzburgite compositions (Ma et al., 2020). When testing the effect of water (Figure S2d), we used a 70 s period and the shear modulus dependence from the seismic study (Priestley & McKenzie, 2013), and assumed dry conditions, 100 wt. ppm water or 200 wt. ppm water in the mantle. We also used the solidus fit from the original work (Yamauchi & Takei, 2016) which has an even lower solidus temperature than the 200 wt. ppm hydrous solidus (Hirschmann et al., 2009). For this conversion approach (Yamauchi & Takei, 2016), water does not directly affect anelasticity, but it instead alters temperature by influencing the pre-melting effect which depends on the solidus temperature. The effects of water and grain size are not directly considered in this relationship, as it is based on an observed

V_S structure which can be assumed to represent the real Earth water and grain size. Some resulting temperatures are unrealistically high because even though these temperatures would result in partial melting which in turn would reduce velocity, these effects are not represented completely in the velocity to temperature scaling (e.g. Figure 2b).

Using the second velocity-temperature conversion approach (Jackson & Faul, 2010) (Figure S2f), we tested the effects of water and grain size. Assuming 100 wt. ppm of water in the mantle, we tested grain sizes of 1 mm and 10 mm. Then assuming 10 mm of grain size, we tested cases with dry mantle and 100 wt. ppm of water. In this case, the water directly affects olivine anelasticity, and we assumed the reference water content in olivine to be 3.125 wt. ppm which was also used in previous work (Abers et al., 2014). A partition coefficient between bulk water and water in olivine was used to obtain the amount of water in olivine (Hirschmann et al., 2009).

During these conversions, pressure is assumed to be the geostatic pressure. To obtain density, we first estimated the Moho depth to be the depth of the maximum velocity gradient depth in the 1D V_S column. Crustal densities were obtained from V_S with an empirical relationship (Shen & Ritzwoller, 2016). Mantle densities were based on density as a function of temperature and pressure from Perple_X (Connolly, 2009), and a harzburgite mantle was assumed for density estimation except for the case where the compositional effect of pyrolite was studied. Since density and pressure depend on each other, an iterative updating of these parameters was applied until they converged.

Among all the different conditions that were tested, the assumed velocity model and the assumed V_S-temperature relationship make the largest impact on inferred temperature (Figure S2). The inferred temperatures vary widely between the different cases, and that is the reason they are not used to estimate mantle potential temperature for this study. However, the inferred temperatures cross the solidus in a similar depth range (Figure S2g-S2i) that overlaps the ~100-150 km depths of the observed positive velocity gradients in the Sp CCP stack. This broad agreement supports our interpretation of the observed positive velocity gradients as the onset of melting.

Text S3. Construction of the Karacadag geotherm

To obtain the geotherm in Figure 3a, we combined a conductive temperature profile $T_{conduction}$ with an adiabatic mantle temperature profile $T_{adiabat}$, with the condition that $T_{geo} = \min(T_{conduction}, T_{adiabat})$. We constructed the temperature profile in this simple way since exact temperatures at the LAB are hard to estimate considering the possibility of ponded melt or other processes (Plank & Forsyth, 2016).

For the mantle adiabat $T_{adiabat}$, we used the thermal expansion coefficients and densities for mantle solid and melt, entropy difference between solid and melt, and heat capacity from previous work (Katz et al., 2003). If the thermodynamic parameters in (Iwamori et al., 1995) are used instead, the estimated T_P value for Karacadag is 15°C higher. Instead of using the hydrous solidus from Katz et al. (2003), we used the solidus from Hirschmann et al. (2009) because it has a relatively complete consideration of compositional effects on water partition coefficients, and the degree of melting was estimated based on a consistent approach (Hirschmann, 2010) (Figure 3b). Although the degree of melting estimates for this approach (Hirschmann, 2010) are primarily for small values, the general trend should be applicable for larger values, and in any case accurate estimation of the degree of melting is not the target of this analysis. We assumed batch melting to calculate the water partition coefficient when melt is present, to avoid complexity when a certain degree of fractional melting is allowed. With all of these assumptions, the adiabatic temperature profile was set up based on relationships in McKenzie (1984).

For the conductive geotherm $T_{conduction}$, the temperature at the LAB depth was assumed to be the dry solidus temperature as assumed in previous work (Plank & Forsyth, 2016). However, if $T_{adiabat}$ was lower than the dry solidus at the LAB depth, $T_{adiabat}$ at the LAB depth was used for the temperature at the LAB. The surface temperature was assumed to be 10°C. The Moho depth was obtained from a previous study (Vanacore et al., 2013) by calculating the average of all Moho depth measurements within 1° distance, and in the Karacadag region, the Moho depth

is 37.75 km. The conductive temperature profile was calculated (Turcotte & Schubert, 2002) for continental crust with radiogenic heat production that exponentially decays with depth. We assumed mantle lithosphere heat generation (Turcotte & Schubert, 2002) of 7.38×10^{-12} Wkg^{-1}; crustal heat generation (Cirmik, 2018) of 1.48×10^{-9} Wkg^{-1} at the surface with exponential decay over a length scale of 8 km; and no asthenospheric heat generation. Mantle and crustal densities (Turcotte & Schubert, 2002) were assumed to be 3.3×10^{3} kgm^{-3} and 2.7×10^{3} kgm^{-3}. The heat conductivities for mantle (Turcotte & Schubert, 2002) and crust (Cirmik, 2018) were 4 $Wm^{-1}K^{-1}$ and 2.5 $Wm^{-1}K^{-1}$.

Text S4. Modeling the transport speed from east Africa to Anatolia

The representative adiabat for the EAR was estimated from deeper basalt samples (Section 5; Figure 11a) and was formulated in the same way as for Karacadag (Supporting Information Text S3). However, the conductive or lithospheric geotherm for the EAR was formulated in a different way, since differences between EAR and Anatolian lithospheres are likely. For the EAR, the conductive geotherm for the lithosphere links the asthenospheric adiabat temperature to 0°C at the surface, and its temperature was assumed to be the dry solidus temperature at 53 km depth which is the upper limit of melting inferred from the distribution of basalt equilibration depths for the north EAR. A 100°C temperature decrease was imposed beneath 200 km depth so that the mantle beneath the channel is at an ambient mantle temperature (Figure 11a). When calculating the lithospheric geotherm, we assumed the whole 40 km thick crust to have an average heat generation of 8.9×10^{-7} Wm^{-3} (Rudnick et al., 2003). Crustal and mantle heat capacities as well as lithospheric heat diffusivity are from (Grose & Afonso, 2013), and mantle lithosphere heat capacity is from (Korenaga & Korenaga, 2016). The crustal density was assumed to be 2.7×10^{3} kg/m^{3}, and mantle density was calculated from Perple_X (Connolly, 2009) assuming a harzburgite composition as in Supporting Information Text S2.

Based on the geotherm and the estimated pressure gradient (Section 5), we calculated the flow speed distribution. During modeling, both stress-dependent dislocation creep and diffusion creep were considered. Above 53 km depth, dry creep laws were assumed, which results in very high viscosities. The 53 km depth limit was based on the north EAR LAB depth, but this choice is not significant since the pressure gradient starts at 100 km depth. For the asthenosphere below 53 km, wet dislocation and diffusion creep flow laws were considered (Hirth & Kohlstedt, 2003). For the 1D pressure-driven Poiseuille flow we are modelling, the governing equation is expressed as

$$\frac{\mathrm{d}\tau(z)}{\mathrm{d}z}=\frac{\mathrm{d}P}{\mathrm{d}x}(z), \tag{1}$$

where τ is the shear stress and $\mathrm{d}P/\mathrm{d}x$ is the horizontal pressure imposed on the mantle. Then, dislocation and diffusion creep flow laws require

$$\frac{\mathrm{d}v}{\mathrm{d}z} = 3^{\frac{(n_{dis}+1)}{2}} A_{dis}(z)\tau\left|\tau\right|^{n_{dis}-1} + 3^{\frac{(n_{dif}+1)}{2}} A_{dif}(z)\tau\left|\tau\right|^{n_{dif}-1}, \quad (2)$$

where v is the horizontal mantle flow speed, and n_{dis} and n_{dif} are the stress dependence of dislocation and diffusion creeps from Hirth and Kohlstedt (2003) which are 3.5 and 1. A_{dis} and A_{dif} are pre-factors from Hirth and Kohlstedt (2003), and both have the form of $AC_{OH}^{r} d^{-p} \exp(-\frac{E+PV}{RT})$, where C_{OH} represents the water content (380 H/10^6Si for 100 wt. ppm), and d is grain size (10 mm), pressure and temperature P and T are from the estimated initial geotherm, and the factors A, r, p the activation energy E and activation volume V are from Hirth and Kohlstedt (2003). However, A for wet creep laws are reduced to 1/3 of their value in Hirth and Kohlstedt (2003) to account for calibrations of FTIR data in olivine (Bell et al., 2003). The term before the pre-factors in eq. (2) are scaling factors to convert the laboratory-defined flow law based on uniaxial compression to simple shear (Paterson & Olgaard, 2000). The effects of partial melt were not considered because the melt fraction is not well-constrained, and ignoring melt makes the test of our modeling approach more conservative, since the transport time would be shorter for a partially-molten less viscous asthenosphere. As is shown in Figure 11a, the combined effects of these terms are reflected by their equivalent viscosity ($\tau \bullet (\mathrm{d}v/\mathrm{d}z)^{-1}$).

The flow speeds were obtained based on eq. (1) and eq. (2). The plate motion at the surface was set to 2 cm/yr as a conservative value from GPlates (Seton et al., 2012) for the last 30 Myr, and the speed at 400 km depth was set to 0. The $\mathrm{d}P/\mathrm{d}x$ profile is shown in Figure 11d. Solutions for the flow based on the simple 1D profile were obtained through integration, and no numerical solvers were used. Based on eq. (1), the shear stress is expressed as $\tau(z) = \int_0^z \frac{\mathrm{d}P}{\mathrm{d}x}(z_1)\,\mathrm{d}z_1 + C_1$, where C_1 is a constant. After substituting τ in eq. (2), and integrating it with depth, the flow speed can be expressed as

193
$$v(z) = 3^{\frac{(n_{dis}+1)}{2}} \int_0^z A_{dis}(z_2)\left(\int_0^{z_2} \frac{\mathrm{d}P}{\mathrm{d}x}(z_1)\,\mathrm{d}z_1 + C_1 \right)\left| \int_0^{z_2} \frac{\mathrm{d}P}{\mathrm{d}x}(z_1)\,\mathrm{d}z_1 + C_1 \right|^{n_{dis}-1} \mathrm{d}z_2 + 3^{\frac{(n_{dif}+1)}{2}} \int_0^z A_{dif}(z_2)\left(\int_0^{z_2} \frac{\mathrm{d}P}{\mathrm{d}x}(z_1)\,\mathrm{d}z_1 + C_1 \right)\left| \int_0^{z_2} \frac{\mathrm{d}P}{\mathrm{d}x}(z_1)\,\mathrm{d}z_1 + C_1 \right|^{n_{dif}-1} \mathrm{d}z_2 + C_2 , \quad (3)$$

194 where C_2 is a constant. To meet the boundary condition at the surface, C_2 is equal to the
195 surface speed (2 cm/yr). C_1 can be found based on the boundary condition that the speed at
196 400 km depth is 0 cm/yr. We performed a grid search of C_1 within the range of
197 $\pm \max\left| \int_0^z \frac{\mathrm{d}P}{\mathrm{d}x}(z_1)dz_1 \right|$ for all z in the range from 0 to 400 km to find the value that results in
198 zero velocity at 400 km depth. With this value, we obtained the flow speed distribution with
199 depth (Figure 11d). The corresponding stress and strain rate were also obtained to find the
200 equivalent viscosity.

201

202

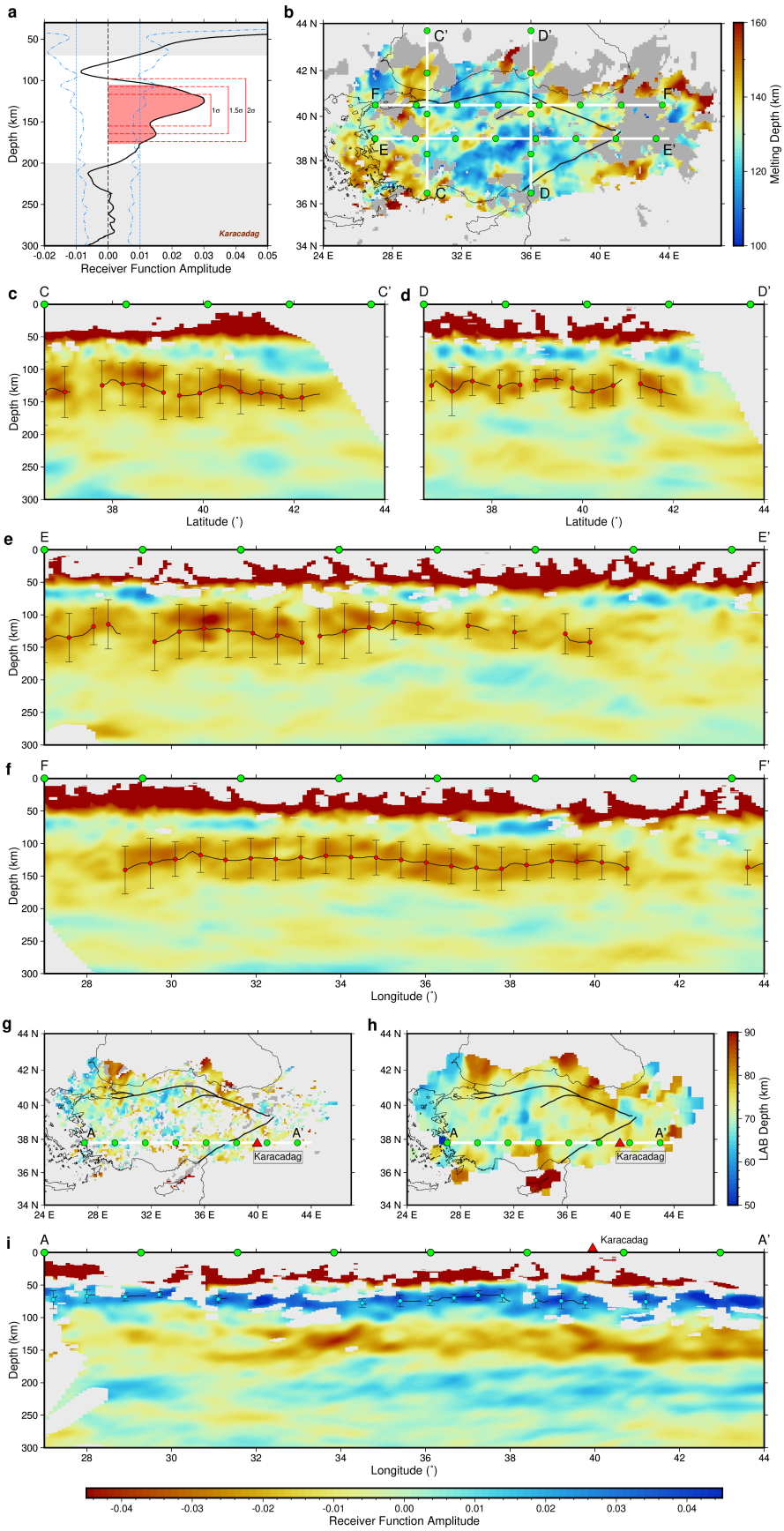
a
Depth (km)
Receiver Function Amplitude
Karacadag
1σ
1.5σ
2σ
b
C'
D'
F
F'
E
E'
C
D
Melting Depth (km)
c
C
C'
Depth (km)
Latitude (˚)
d
D
D'
Latitude (˚)
e
E
E'
Depth (km)
f
F
F'
Depth (km)
Longitude (˚)
g
A
A'
Karacadag
h
A
A'
Karacadag
LAB Depth (km)
i
A
Karacadag
A'
Depth (km)
Longitude (˚)
Receiver Function Amplitude

Figure S1. Sp receiver function stacks for the Anatolian region. (a) Example of picking negative Sp phases from a location in the Karacadag volcanic field. The sign for the receiver function amplitude (black thick line) is flipped to be consistent with the Ps convention. The dotted line shows 0.01 amplitude, and the dotted-dashed line shows twice the amplitude standard deviation. Depths not used for picking are shown in gray. Red shading denotes the phase probability distribution. Red bars show depth ranges if using one, one and half or two times the picked phase depth standard deviation to represent depth extent. (b) Similar to Figure 1a, with cross-section locations for (c) to (f) labelled. (c)-(f) Sp common-conversion point stack amplitude (10-100 s bandpass filter) with the color bar at the bottom of figure. Picked phase depths are shown by black lines with red markers. Half of the error bar lengths show the 1.5 standard deviation of phase depth, which marks half of the phase depth extent. (g) Picked LAB (positive phase) depths. (h) Smoothed LAB depth distribution. (i) Cross-section A-A′ for the stack with a 2-20s bandpass filter. Picked LAB phases shown by black lines with blue marker. Half of the error bar lengths show one standard deviation of phase depth.

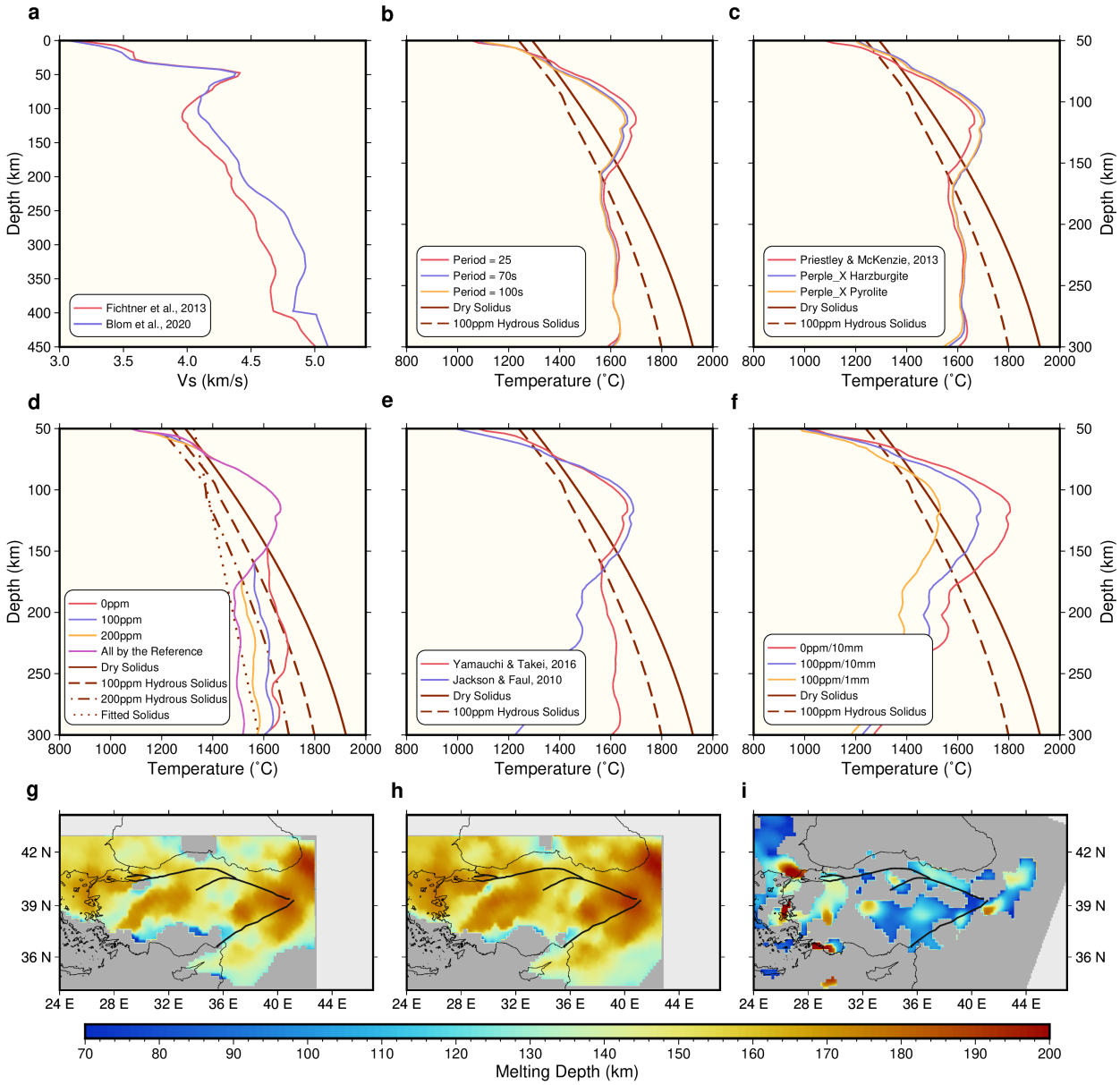

Figure S2. V_S-temperature conversion. The conversion here serves purely to demonstrate the observed Sp phases correspond to the melting depth, and no further interpretations are made based on these widely-spread converted temperatures. (a) The same as Figure 2a. (b)-(f) Temperature converted from V_S in (a); dry and 100 wt. ppm hydrous solidii (Hirschmann et al., 2009) are shown by solid and dashed dark red lines. Legends show the conditions assumed when converting velocity to temperature. (b)-(d) Conversions are based on the V_S-temperature relationship in Yamauchi and Takei (2016), while (f) is based on Jackson and Faul (2010). (b) Testing the effects of assumed V_S frequencies. (c) Testing the effect of assumed

compositions. (d) Testing the effect of assumed mantle water content as well as the inferred mantle solidus in the original V_S-temperature relationship work (Yamauchi & Takei, 2016) (purple lines). (e) Testing the effect of the V_S-temperature relationship. (f) Testing direct effects of water and grain sizes. (g)-(i) Melting depth distribution from V_S with a 100 wt. ppm hydrous mantle, based on: g) the local velocity model (Fichtner et al., 2013) and the V_S-temperature relationship in Yamauchi and Takei (2016); h) the local velocity model (Fichtner et al., 2013) and the V_S-temperature relationship in Jackson and Faul (2010); and i) the regional velocity model (Blom et al., 2020) and the V_S-temperature relationship in Yamauchi and Takei (2016).

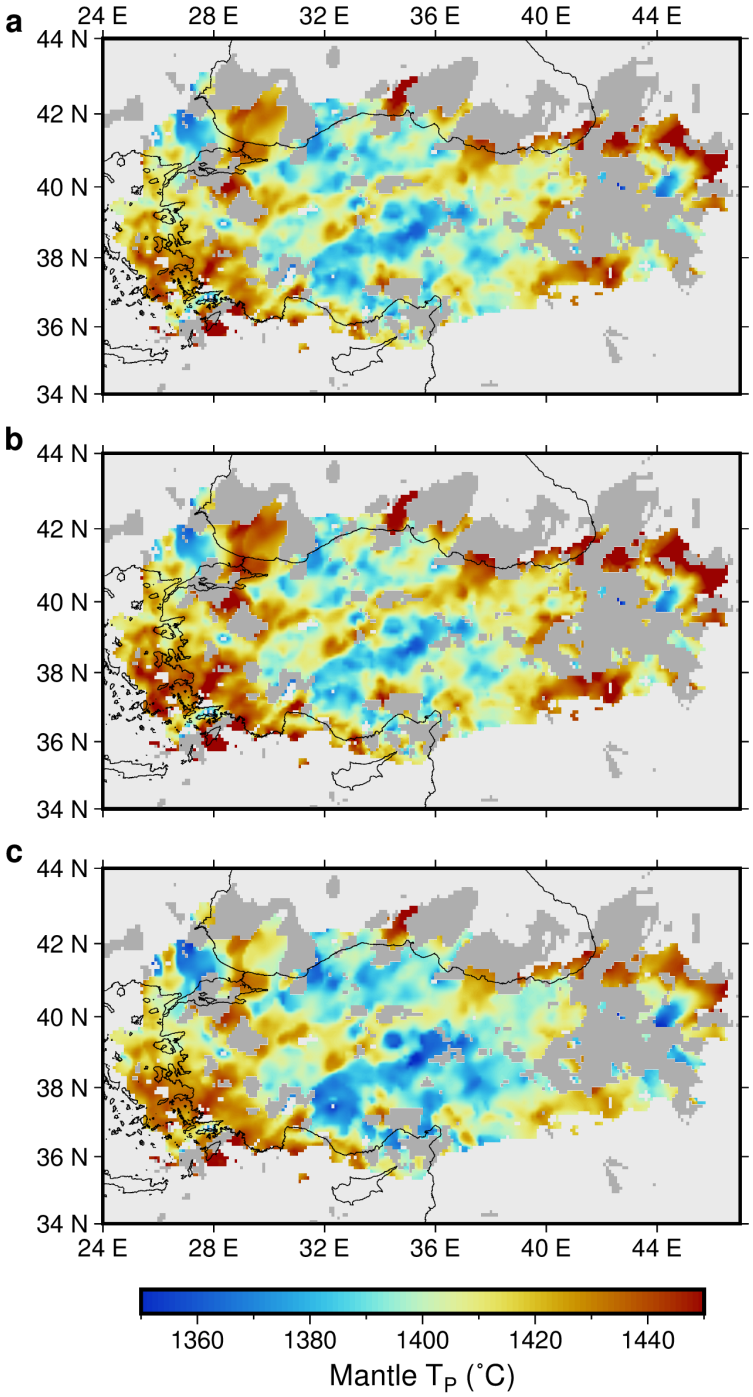

238

239 **Figure S3.** Mantle T_P determination for Anatolia. (a) Mantle T_P estimated across Anatolia based
240 on melting onset depths from the Sp stack and mantle with 100 wt. ppm water. (b) Similar to
241 (a) but based on the scenario in Figure 6a & 6b. (c) Similar to (a) but based on the scenario in
242 Figure 6c & 6d.

243

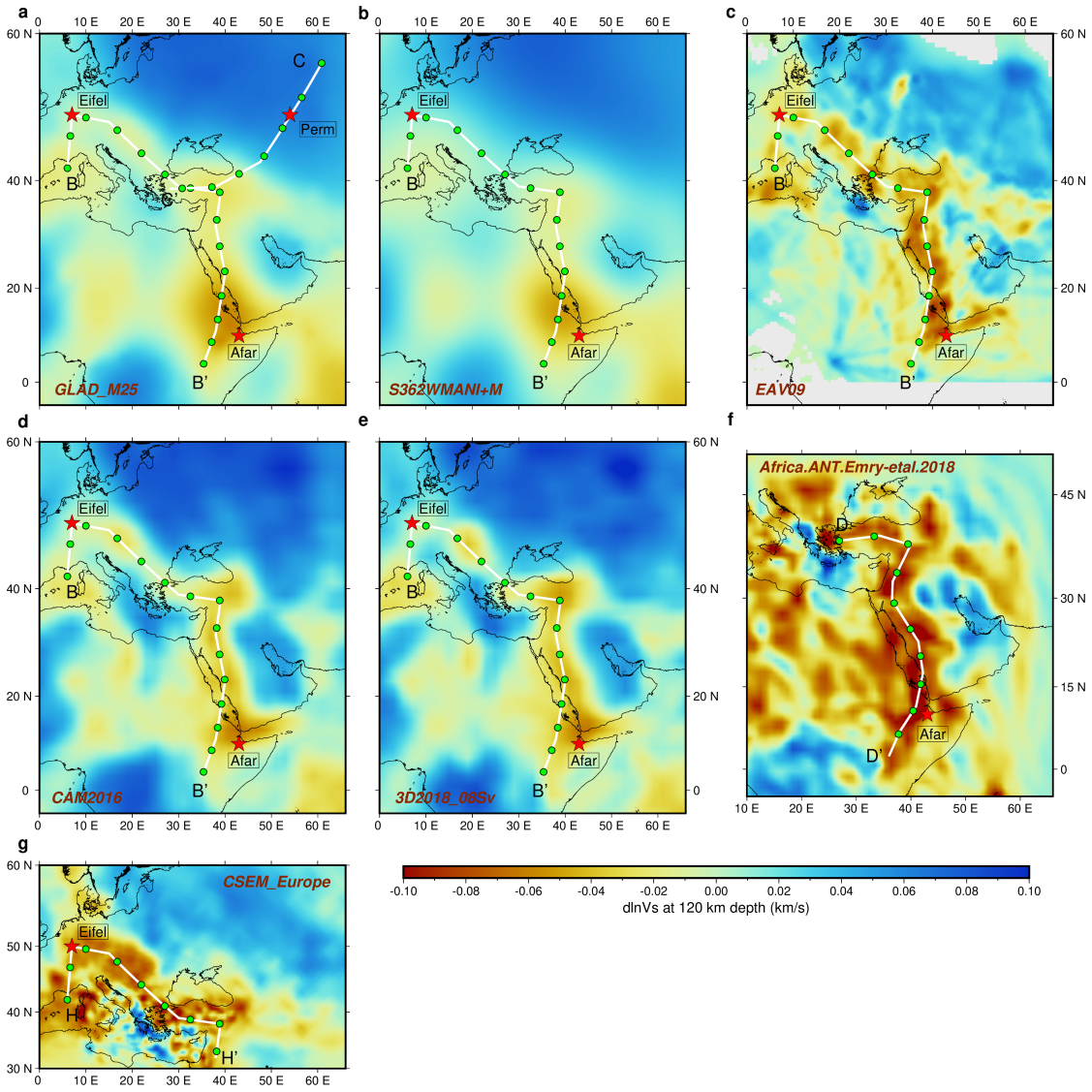

Figure S4. Shear velocity perturbation at 120 km depth from multiple models, similar to Figure 7a. Perturbations were calculated with respect to the average velocity at each depth. Locations of cross-sections shown in Figure S5 are indicated by white lines with green markers. Velocity models (also labeled in panels) are GLAD_M25 (Lei et al., 2020) in (a), S362WMANI+M (Moulik & Ekström, 2014) in (b), EAV09 (Chang et al., 2010) in (c), CAM2016 (Ho et al., 2016) in (d), 3D2018_08Sv (Debayle et al., 2016) in (e), Africa.ANT.Emry-etal.2018 (Emry et al., 2019) in (f) and CESM_Europe (Fichtner et al., 2018) in (g). For velocity models that provide V_S, those values are shown. For models that provide both V_{SV} and V_{SH}, the Voigt average was applied to obtain isotropic V_S. For models with only V_{SV}, that value is shown.

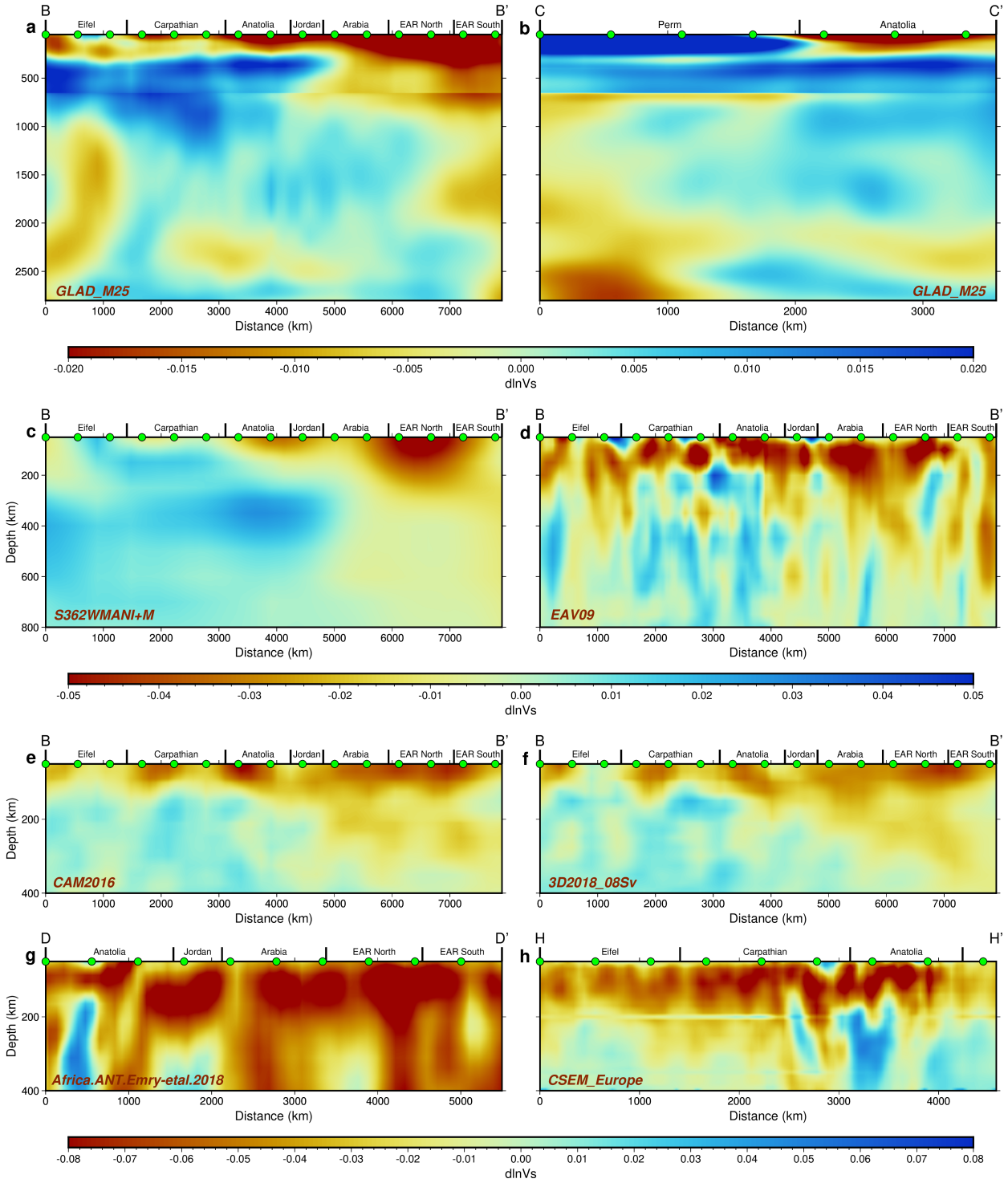

Figure S5. Mantle V_S perturbation cross-sections. Cross-section locations are shown in Figure S4. Perturbations are calculated with respect to the average velocity at each depth. Names of the velocity models are indicated in the panels. Velocity models (also labeled in panels) are GLAD_M25 (Lei et al., 2020) in (a) and (b), S362WMANI+M (Moulik & Ekström, 2014) in (c), EAV09

(Chang et al., 2010) in (d), CAM2016 (Ho et al., 2016) in (e), 3D2018_08Sv (Debayle et al., 2016) in (f), Africa.ANT.Emry-etal.2018 (Emry et al., 2019) in (g) and CESM_Europe (Fichtner et al., 2018) in (h). Geochemical sample geographic group ranges and the surface projections of the Eifel hotspot and Perm anomaly are labelled at the top. Green symbols correspond to the same symbols in Figure S4. Color bars for groups of panels are given below each group. The minimum depth in each panel is 50 km.

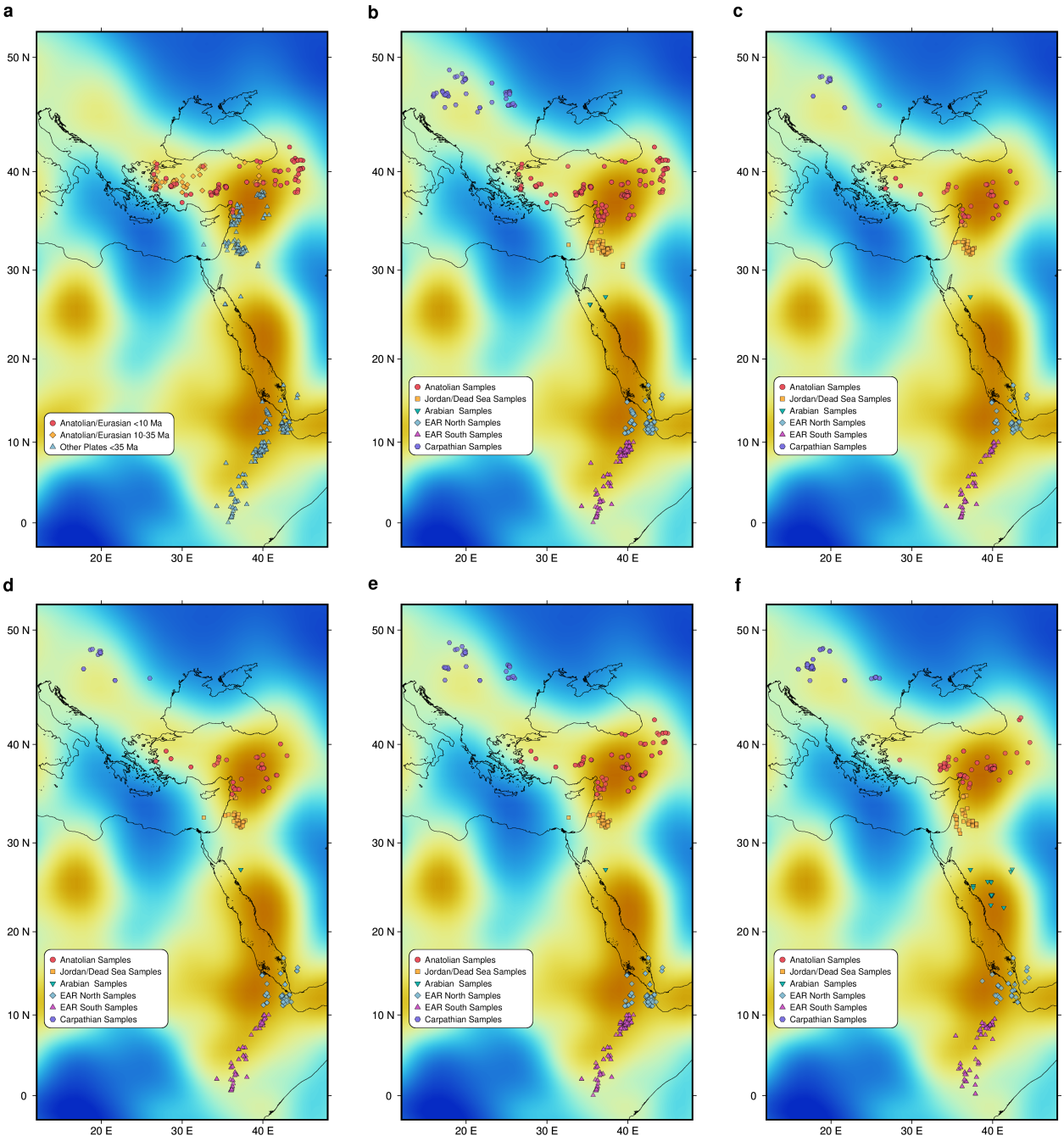

267

268 **Figure S6.** Distribution of basaltic samples. The base V_S map is the same as in Figure 8a. Symbols
269 on this plot match symbols in Figure 8, 9 & S7. (a) Samples used in Figure 8B. (b) Samples used
270 in Figure S7c. (c) Samples used in Figure 8d & S7d. (d) Samples used in Figure 8e & S7a. (e)
271 Samples used in Figure S7b. (f) Samples used in Figure 9.

272

273

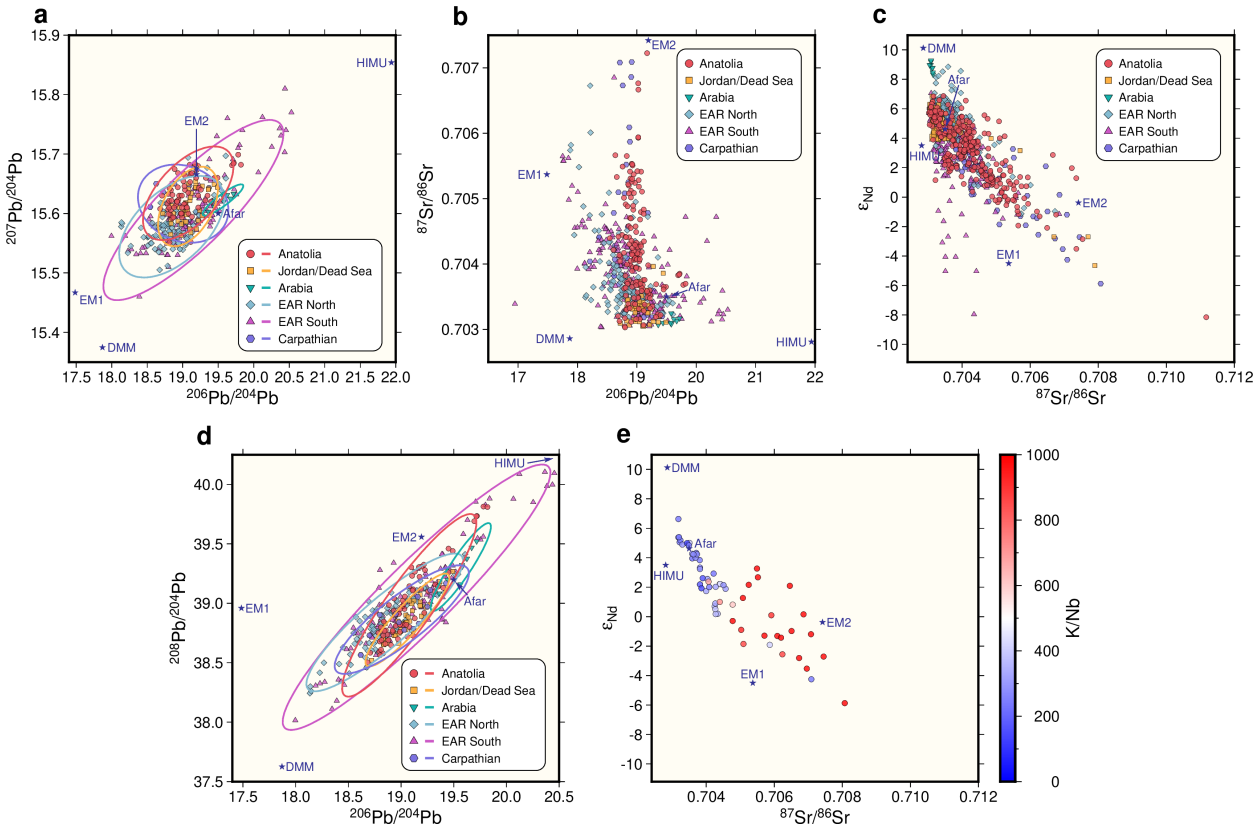

274

275 **Figure S7.** Radiogenic isotope analyses. Stars show mantle endmembers (Hofmann, 2007) and
276 the Afar plume composition (Rooney et al., 2012). (a) $^{206}Pb/^{204}Pb$ vs. $^{207}Pb/^{204}Pb$, similar to Figure
277 8e but with Carpathian samples. (b) $^{206}Pb/^{204}Pb$ vs. $^{87}Sr/^{86}Sr$. (c) $^{87}Sr/^{86}Sr$ vs. ε_{Nd}, similar to Figure
278 8b, except that data are divided into geographic groups and include Carpathian samples, while
279 samples > 10 Ma from the Anatolian plate are not included. (d) $^{206}Pb/^{204}Pb$ vs. $^{208}Pb/^{204}Pb$, similar
280 to Figure 8d, but with Carpathian samples. (e) Similar to Figure 8b, but for samples in the
281 Carpathian group after 10 Ma.

282

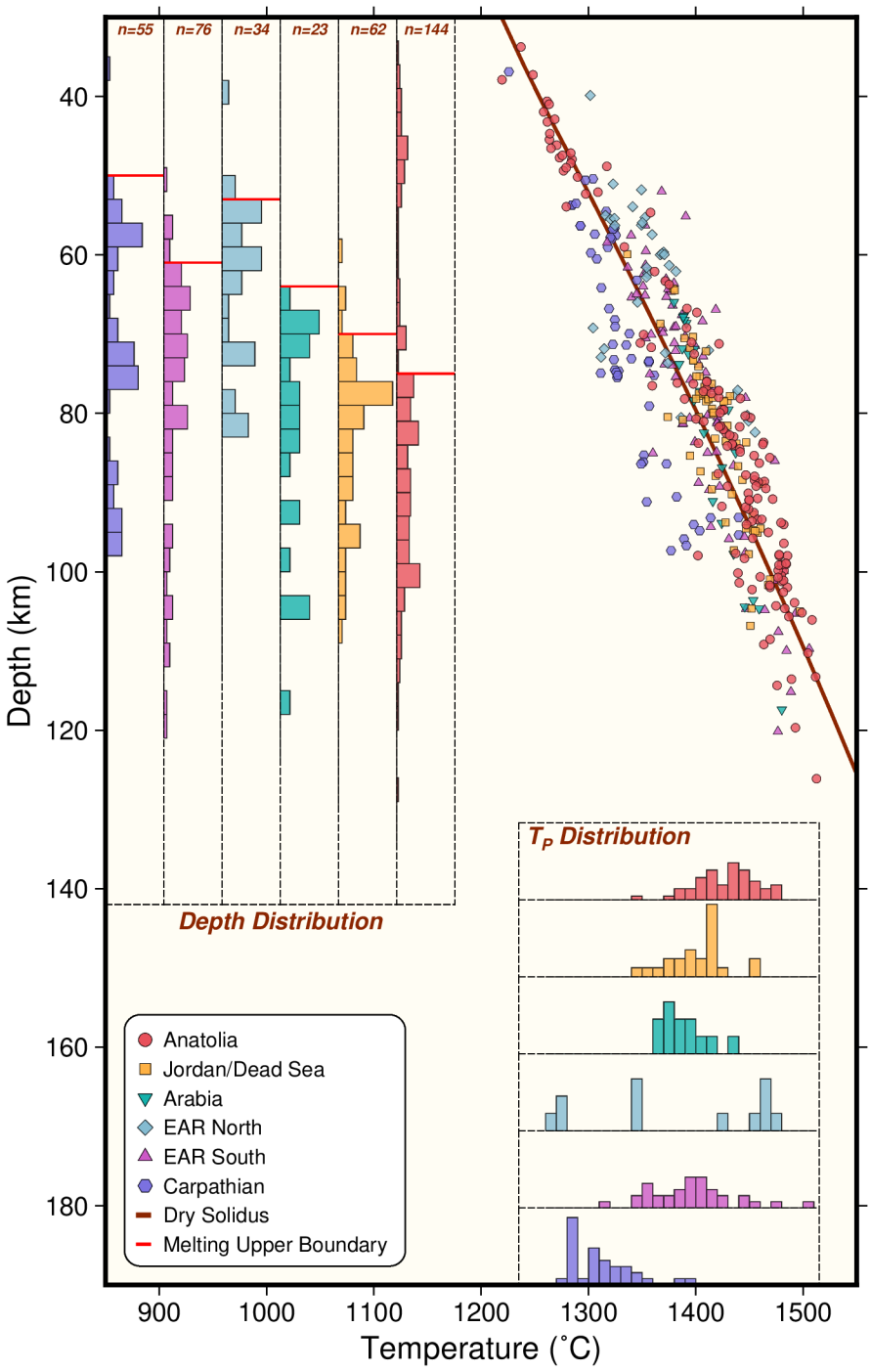

283

284 **Figure S8.** Primary magma equilibration conditions. Similar to Figure 9a, except here only
285 samples with normalized MgO higher than 9 wt. % are included instead of 8 wt. %.

286

287

Data Set S1. (ds01.xlsx)

Information about the samples we used to calculate primary magma equilibration conditions.

Data Set S2. (ds02.xlsx)

Information about the samples we used to analyze their isotopic signatures.

Data Set S3. (ds03.xlsx)

References for the original works of the samples.